AVS Quantum Science

PERSPECTIVE | APRIL 27 2022

A roadmap for universal high-mass matter-wave interferometry

Special Collection: Celebrating Sir Roger Penrose's Nobel Prize

Filip Kiałka ; Yaakov Y. Fein ; Sebastian Pedalino ; Stefan Gerlich ; Markus Arndt

Check for updates

AVS Quantum Sci. 4, 020502 (2022)
https://doi.org/10.1116/5.0080940

View Online
Export Citation

Articles You May Be Interested In

Roadmap on material-function mapping for photonic-electronic hybrid neural networks

APL Mater. (October 2019)

Closing the loop on glioblastoma: A roadmap toward developing bioelectronics for continuous monitoring of tumor state

APL Bioeng. (March 2026)

Industry perspective: Limits of energy efficiency for conventional CMOS and the need for adiabatic reversible computing

08 May 2026 15:38:38

AIP Publishing

AVS Quantum Science PERSPECTIVE scitation.org/journal/aqs

A roadmap for universal high-mass matter-wave interferometry

Cite as: AVS Quantum Sci. 4, 020502 (2022); doi: 10.1116/5.0080940
Submitted: 5 December 2021 · Accepted: 6 April 2022 ·
Published Online: 27 April 2022

View Online Export Citation CrossMark

Filip Kiałka,[1] Yaakov Y. Fein,[1] Sebastian Pedalino,[1,2] Stefan Gerlich,[1] and Markus Arndt[1,a)]

AFFILIATIONS

[1]Faculty of Physics, University of Vienna, Boltzmanngasse 5, A-1090 Vienna, Austria
[2]Vienna Doctoral School in Physics, University of Vienna, Boltzmanngasse 5, A-1090 Vienna, Austria

Note: This paper is part of the special topic Celebrating Sir Roger Penrose's Nobel Prize.
[a)]**Electronic mail:** markus.arndt@univie.ac.at

ABSTRACT

Creating quantum superposition states of bodies with increasing mass and complexity is an exciting and important challenge. Demonstrating such superpositions is vital for understanding how classical observations arise from the underlying quantum physics. Here, we discuss how recent progress in macromolecule interferometry can be combined with the state of the art in cluster physics to push the mass record for matter-wave interference with wide state separation by 3 to 4 orders of magnitude. We show how near-field interferometers in different configurations can achieve this goal for a wide range of particle materials with strongly varying properties. This universality will become important in advanced tests of wave function collapse and of other modifications of quantum mechanics, as well as in the search for light dark matter and in tests of gravity with composite quantum systems.

© 2022 Author(s). All article content, except where otherwise noted, is licensed under a Creative Commons Attribution (CC BY) license (http://creativecommons.org/licenses/by/4.0/). https://doi.org/10.1116/5.0080940

08 May 2026 15:38:38

I. INTRODUCTION

A. Historical context and state of the art

Louis de Broglie's hypothesis[1] that even massive particles have an associated wavelength inspired Erwin Schrödinger's formulation of quantum wave mechanics.[2] Key aspects of the theory were experimentally confirmed soon after its publication, with the diffraction of electrons in 1927,[3,4] helium atoms and hydrogen molecules in 1930,[5] and neutrons in 1936.[6] Coherent beamsplitters for atoms were developed 50 years later,[7–13] giving rise to the now-mature field of atom interferometry.[14,15] Atom interferometry has found applications in precision gravimetry, with applications in geodesy, prospection of natural resources, and inertial navigation. On the more fundamental side, it has been used in tests of general relativity,[16,17,95] searches for dark matter[18] and dark energy,[19,20] and precision measurements of fundamental constants.[21,22]

In this contribution, we explore methods to create superpositions of objects that are larger, more massive and more complex than single atoms or dimers. This research program began with a far-field diffraction of the fullerenes C_{60} and C_{70},[23] followed by the realization of a Talbot–Lau Interferometer (TLI),[24] a Kapitza–Dirac–Talbot–Lau interferometer for large organic molecules,[25] and time-domain interferometry with pulsed photo-depletion gratings.[26] The most massive particles to exhibit quantum interference to date are functionalized oligoporphyrins with a mass of 27 kDa, consisting of nearly 2000 atoms.[27] This was achieved in the Long-baseline Universal Matter-wave Interferometer (LUMI), a two-meter baseline Talbot–Lau scheme, which combines features of several previous experiments.

LUMI holds the mass record among experiments in which delocalization is confirmed by subsequent matter-wave interference. Molecule interferometry is also the platform in which the most massive particles have been delocalized over a distance comparable to or larger than their size. There are also a growing number of experiments probing macroscopic quantum mechanics from a number of different angles, covering masses from atoms in superpositions as wide as half a meter[28] to correlated modes of macroscopic objects as massive as 10 kg in the case of the mirrors of the LIGO (Laser Interferometer Gravitational-Wave Observatory) experiment.[29] Enormous progress has also been made in gaining quantum control over mesoscopic particles, such as glass beads cooled to the quantum ground state of optical traps.[30–32] There are also proposals for quantum experiments with massive superconducting spheres[33] and nanodiamonds with implanted NV centers,[34] the latter with a particular focus on tests of quantum gravity. One may also explore rotational rather than linear state space, with some conceptual and practical advantages.[35,36] Such experiments and proposals are contributing to the rapid advances in testing quantum physics on an increasingly macroscopic scale.[37,38]

© Author(s) 2022.

B. Modifications of standard quantum mechanics

The results of all experiments so far support the same conclusion, namely, that quantum physics is the correct theory for isolated atoms and molecules. Such experiments force us to question the concepts of reality and locality with which we are familiar in our "classical world." This question has also intrigued Roger Penrose for several decades,[39] and we celebrate his pioneering work on the occasion of his Nobel Prize with ideas on how to test quantum physics at the border with classical physics.

While standard quantum mechanics remains the uncontested leading theory for describing nature on the microscopic scale, alternative models have been proposed, which extend quantum mechanics via additional, usually non-linear, terms, while remaining compatible with the increasingly stringent bounds placed by experiments. This includes models of objective wave function collapse, which were introduced by Ghirardi *et al.*[40,41] and generalized to gravity-induced collapse models by Diosi[42] and Penrose.[39] Aspects of such collapse would also arise in solutions of the Newton–Schrödinger equation,[43] a semi-classical approach to combining quantum and gravitational theory. The incompatibility of quantum mechanics with general relativity has triggered investigation into how space-time fluctuations could influence macroscopic mass superpositions[44,45] and how gravitational redshift can lead to state dephasing and effective decoherence of particles with internal electronic or vibrational clocks.[46,47]

A common feature of these models is that classical features emerge as the mass m of the superposed object grows. Many models predict an initial scaling with m^2, but also with the coherence time and width of the spatial superposition state or with the number of internal degrees of freedom. This provides a strong motivation to demonstrate the delocalization of increasingly massive objects, since interference experiments place robust experimental bounds on such models.[48]

C. Talbot–Lau interferometry

In this work, we focus on a bottom-up approach to matter-wave interferometry with masses up to 100 MDa, bridging the mass gap to the dielectric particles currently used in state-of-the-art cooling experiments. We apply ideas from atom and molecule interferometry to massive metal clusters, in particular, making use of the near-field Talbot–Lau effect, described below.

Near-field self-imaging of periodic structures dates back to observations by Henry Fox Talbot in 1836 in the context of classical optics.[49] The scheme was extended to the self-imaging of spatially incoherent sources by Lau in 1948.[50] The suitability of such schemes for matter-wave interferometry was first realized and demonstrated by John Clauser,[51,52] and related concepts have been used to extend molecule interference experiments to their current state of the art.[25–27]

In the basic Talbot–Lau effect, a molecular beam passes two sequential gratings, and near-field interference causes a density modulation to develop in the beam after the second grating. Detection of this interference pattern is typically achieved by scanning an additional third grating perpendicularly to the fringes and measuring the transmitted particle flux with a non-spatially resolving detector.

The key advantage of a TLI compared to far-field setups, such as the Mach–Zehnder interferometer, is the scaling of the period of the interference pattern with $1/\sqrt{m}$, compared to $1/m$ for far-field setups. Additionally, TLIs exhibit significantly relaxed requirements on the initial transverse coherence of the particle beam. This is important in high-mass interferometry as it allows one to conserve the experimentally limited flux by eliminating the need for narrow collimation. Finally, the detection of the pattern by means of a scanning grating allows for the measurement of interference fringes with periods smaller than the optical diffraction limit and for the use of particles that cannot be imaged with conventional microscopy techniques.

Talbot–Lau schemes are also universal in the sense that they accept a wide range of molecular beam sources, and the typical grating mechanisms are off-resonant. In the LUMI experiment, in particular, this has been exploited in metrology experiments on a range of particle types, including atoms,[53] fullerenes,[54] hydrocarbons,[55] and functionalized tripeptides.[56] Such universality is also what allows us now to propose extending the scheme to metal clusters, a new class of particles for matter-wave interference.

Increasing the mass in TLI schemes beyond the current record requires innovations in the formation of neutral, intense, and intact molecular beams as well as in grating technology. Additionally, since higher mass particles necessitate longer evolution times in the interferometer, optimizing the interferometer configuration is also critical.

In this contribution, we propose a number of interferometer schemes compatible with metal cluster beams and photodepletion gratings. Such gratings have already been demonstrated in the time domain,[26] and intense metal cluster beams are routinely employed in cluster physics.[57] We show how an all-optical upgrade of LUMI will enable the interference of metal clusters with masses of up to 10^6 Da. We also propose a successor experiment: a near-field all-optical fountain interferometer, pushing the particle mass and the superposition time by at least another order of magnitude.

The paper is organized as follows: In Sec. II, we discuss some of the key design choices that have to be made while planning the next generation of high-mass TLIs. Section III discusses limits imposed by dephasing and decoherence mechanisms. In Sec. IV, we briefly discuss the technical aspects and suggest a roadmap to universal, high-mass, matter-wave interference.

II. DESIGN OF UNIVERSAL TALBOT–LAU INTERFEROMETERS

A. The number of diffraction gratings

Talbot–Lau interferometers typically consist of three gratings, but viable schemes with either fewer or more gratings have been proposed. In particular, direct imaging of an interference pattern deposited on a surface can replace the third grating and a counting detector,[58] resulting in a two-grating interferometer with increased transmission. Going further, a single-grating Talbot interferometer can be realized if a cold and well-localized source is available.[59] On the other hand, schemes with four and more gratings are also viable and can reduce the sensitivity of the interferometer to Coriolis acceleration.[60]

In the following discussion, we will focus on three-grating Talbot–Lau interferometers. Their advantage over schemes with more gratings is the smaller total duration of the interference scheme, which makes them more suitable for the interference of highly massive particles in free fall. Two-grating schemes remain a promising alternative that will be explored in more detail as label-free super-resolution imaging techniques mature.

08 May 2026 15:38:38

© Author(s) 2022

B. The type of diffraction gratings

The current mass record has been achieved on a TLI consisting of two nanomechanical masks and one optical phase grating.[27] Using mechanical gratings allows one to reach optimal signal-to-noise ratios in many cases,[61] but dispersion forces[62] and mechanical clogging[63] pose challenges and will even render such gratings opaque for many particles beyond the 10^4 Da mass range. This makes mechanical gratings sub-optimal for the interference of very massive particles and compels us to consider interferometers consisting of only optical gratings.

Optical gratings for matter waves can be realized using standing waves of laser light. They can modulate only the phase, or both the phase and the amplitude of the matter wave. The phase modulation results from the interaction of polarizable particles with the light field via the dipole force. To additionally obtain transmission modulation, it is necessary to post-select the particles, which have or have not absorbed a grating photon. The post-selection is the most straightforward, if the charge or mass of the particles changes upon photon absorption, for example, as a result of photocleavage,[64] ionization,[26] or fragmentation.[65] The separation of charge or mass classes can then be achieved using static electric fields either directly[26] or after ionization in a mass spectrometer.[65] Because the probability of photon absorption is a function of the intensity of light, the period of a standing-wave optical grating is half the wavelength of the grating laser.

The first and the third gratings of a TLI must be transmission gratings to prepare transverse coherence and to mask the interference pattern, respectively. The inner grating, on the other hand, can be either a transmission or a phase grating. The latter is often advantageous as it results in an increased transmission of the interferometer and can shorten the total duration of the interferometric sequence thanks to microlensing. However, alternating optical depletion and phase gratings are not easily achieved using a single laser wavelength, and combining different wavelengths is subject to restrictive conditions.[66] We will, thus, focus on interferometer designs using three optical transmission gratings with equal periods.

The transmission t and the sinusoidal visibility V of the interference pattern in a TLI consisting of three depletion gratings are given by[67]

$$t = e^{-(n_1+n_2+n_3)/2} I_0\left(\frac{n_1}{2}\right) I_0\left(\frac{n_2}{2}\right) I_0\left(\frac{n_3}{2}\right), \tag{1}$$

$$V = \frac{2I_1(n_1/2)I_1(n_3/2)}{I_0(n_1/2)I_0(n_3/2)} \left|\frac{\beta\cos(\pi\tau) - \sin(\pi\tau)}{\beta\cos(\pi\tau) + \sin(\pi\tau)}\right| \times \left|J_2\left(\frac{n_2}{2\beta}\sqrt{\sin^2(\pi\tau) - \beta^2\cos^2(\pi\tau)}\right)\right|, \tag{2}$$

where I and J are the Bessel functions of the first kind, n_1, n_2, n_3 are the mean numbers of photons absorbed at the antinodes of the first, second, and third grating, β is a material constant, and τ is the flight time T between the gratings in units of Talbot time T_T for a particle with mass m and a grating with period d,

$$\tau = \frac{T}{T_T} = T\frac{h}{md^2}. \tag{3}$$

The material constant, $\beta = n/2\phi$, is given by the ratio of the number of absorbed photons to the phase ϕ imprinted upon the particle at the antinode of the optical grating.[67] It can be both positive and negative, depending on the sign of the polarizability of the particle, which is positive for high-field seekers and negative for low-field seekers. To capture both possibilities in a continuous fashion,[68] we will refer to the inverse,

$$\beta^{-1} = \frac{2\phi}{n} = \frac{8\pi^2\alpha'}{\sigma\lambda}, \tag{4}$$

where α', σ are the polarizability volume and absorption cross section of the particle at the grating wavelength $\lambda = 2d$.

In a near-field interferometer, the occurrence of a fringe pattern does not necessarily imply that quantum interference has taken place. That is, because classical shadowing and optical lensing can both lead to the appearance of fringe-like caustics. It is, therefore, important to compare the visibility of the observed pattern to both quantum and classical expectations. The classical expectation emerges from Eq. (2) in the limit of short propagation times, which is obtained by replacing $\cos(\pi\tau) \to 1$ and $\sin(\pi\tau) \to \pi\tau$. The transmission of the interferometer is the same in the quantum and classical cases.

Equations (1) and (2) simplify if external gratings use equal laser intensities, that is, if

$$n_1 = n_3 = n_{13}. \tag{5}$$

Under the assumption of constant laser power, $n_1 + n_3 = \text{const.}$, taking $n_1 = n_3$ maximizes pattern visibility but minimizes the interferometer transmission (see Fig. 1). Since the shot noise in the interferometer is proportional to the square root of the number of counts (and thus to the square root of the transmission), the optimal balance between visibility and transmission is found by optimizing the signal-to-noise ratio,[61]

$$\text{SNR} \propto V\sqrt{t}. \tag{6}$$

As illustrated in Fig. 1, the above quantity is optimal at $n_1 = n_3$ and essentially saturates at

$$n_{13} \lesssim 4. \tag{7}$$

Because the factor in front of the absolute values in Eq. (2) does not depend on n_2, the free-flight τ corresponding to maximal pattern visibility will depend only on n_2 and β. The optimal τ can be found by numerical optimization and is smaller than unity for positive β and larger than one for negative β (see Fig. 2). This dependence is a result of the optical dipole force, respectively, focusing or defocusing the Talbot pattern. Because of the defocusing effect, low-field seeking particles are not optimal for high-mass interference, in which the length of the interferometer is typically a major limiting factor. In the examples later in the text, we will assume $\tau = 0.85$, which corresponds to moderate positive β.

Furthermore, as the prefactor in Eq. (2) is the same in the quantum and in the classical cases, the ratio of quantum to classical visibility is also determined only by n_2 and β (assuming quantum-optimal τ). For all but small negative β^{-1}, the quantum-to-classical ratio can be guaranteed to exceed 2 if $n_2 \geq 2.5$ (see Fig. 2). The absolute value of quantum visibility can be changed without affecting the quantum-to-classical ratio by adjusting n_{13}. The value of n_{13} corresponding to $V = 50\%$ is shown in Fig. 2, together with the resulting interferometer transmission. We find that using $n_2 < 3.5$, while sufficient to obtain a

08 May 2026 15:38:38

© Author(s) 2022

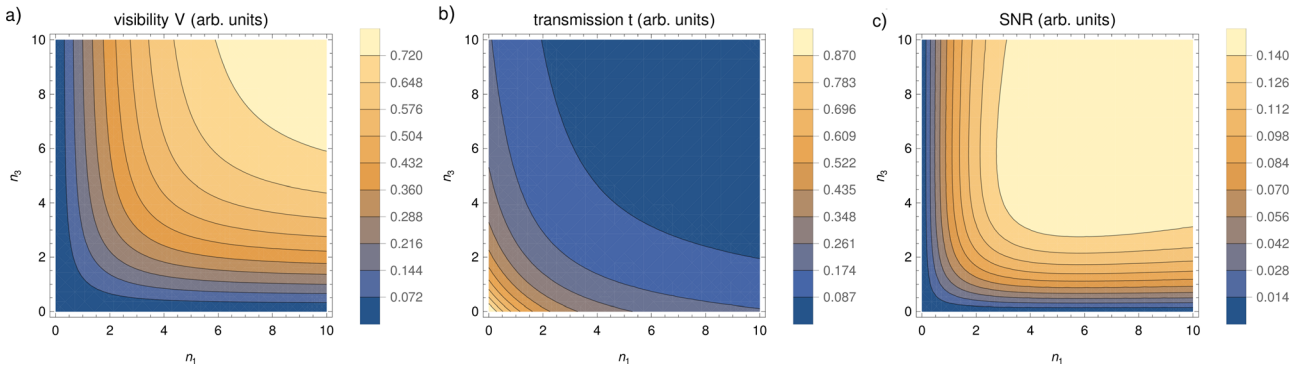

FIG. 1. The dependence of visibility (a), transmission (b), and signal-to-noise ratio (c) on the mean number of photons absorbed at the antinodes of the first and last grating in a TLI with three optical depletion gratings.

quantum-to-classical ratio of 2, would require prohibitively large n_{13} to reach a visibility of 50%. However, taking

$$n_2 \gtrsim 3.5, \tag{8}$$

guarantees a good quantum-to-classical visibility ratio with the former exceeding 50% for all but small negative β^{-1}.

Taken together, Eqs. (7) and (8) imply that the absorption of about 10 photons per particle passing through the antinodes of the gratings is sufficient for operating a TLI near the optimal conditions for a range of particle materials. This can serve as a quick guideline regarding the necessary grating laser intensity.

Finally, Eq. (2) is only valid for a symmetric interferometer, that is, one in which the flight times T_1, T_2 after the first and the second grating are equal, $T_1 = T_2 = T$. Imperfect alignment or (in the case of a vertical interferometer) gravitational acceleration can lead to an asymmetry of the timing. For an interferometer with equal grating periods, the asymmetry can be quantified using

$$s = \frac{T_1 - T_2}{T_T} d. \tag{9}$$

For $s \neq 0$, the visibility is suppressed by a factor $\tilde{D}(s)$, where $\tilde{D}$ is the Fourier transform of the initial transverse momentum distribution of the molecular beam.[60] The latter can be assumed to be Gaussian with a standard deviation of $\hbar/\sigma_p$, where $\sigma_p \approx mv\theta$ is approximately given by the initial forward velocity v and the collimation angle θ. Thus, the presence of a timing asymmetry limits the acceptance angle to

$$\theta \ll \frac{d}{2\pi v|T_1 - T_2|}. \tag{10}$$

C. Arrangement of the gratings

The three gratings of a TLI can be arranged in a number of ways, as shown in Fig. 3. The configurations differ primarily in their longitudinal velocity acceptance, which is usually limited by the dispersion of the classical particle trajectories. Maximizing velocity acceptance is necessary for compatibility with established high-flux beam sources, such as magnetron sputtering, which give rise to broad velocity spectra.

1. Horizontal particle beam, continuous transverse gratings

This is the configuration used in LUMI and in most previous molecular TLIs: the interferometer is horizontal and the gratings are perpendicular to the particle beam and not pulsed. The forward

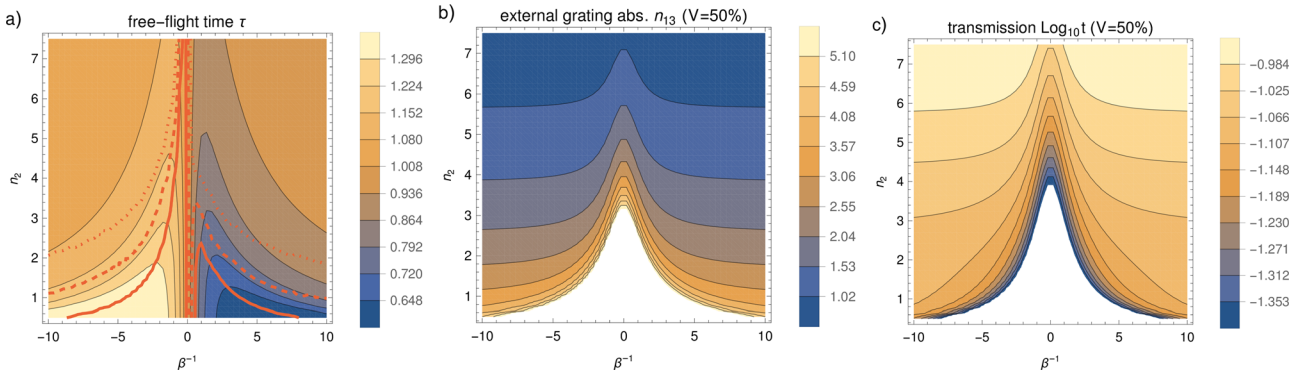

FIG. 2. (a) Grating separation τ (in units of Talbot time) resulting in optimum visibility in a triple-depletion TLI. The red continuous, dashed, and dotted contours correspond to the quantum visibility exceeding the classical one by a factor of 2, 5, and 10, respectively. (b) Number of photons absorbed at the antinodes of the external grating necessary to achieve a quantum visibility of 50%, assuming optimal τ from the left figure. (c) Interferometer transmission for a quantum visibility of 50% and optimal τ.

08 May 2026 15:38:38

© Author(s) 2022

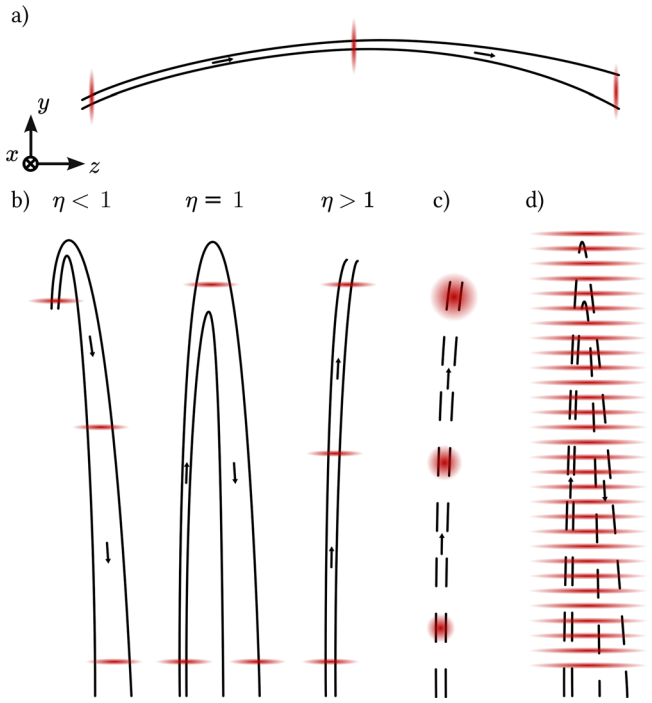

FIG. 3. Examples of possible three-grating Talbot–Lau interferometer arrangements: (a) horizontal particle beam with continuous, transverse gratings; (b) vertical particle beam with continuous, transverse gratings; (c) vertical particle beam with pulsed, transverse gratings; and (d) vertical particle beam with pulsed, longitudinal grating.

velocity acceptance of this scheme is determined by geometric and dynamical constraints. The former arises due to the finite extent of the gratings, and the latter because the evolution times between the gratings must be equal and close to τT_T.

The most immediate geometrical constraint results from the vertical drop of the molecular beam. Assuming the particles are launched slightly upward so that they peak in the middle of the interferometer, the total height of the apparatus must exceed

$$H = \frac{gT^2}{2}, \tag{11}$$

where T is the desired free-evolution time between the gratings. Another constraint results from the vertical dispersion of the molecular beam at the position of the third grating. To find the latter, we assume initial velocity components $v_y = (1+\delta)gT$, $v_z = (1+\delta)L/T$, where δ is the relative velocity deviation and L is the fixed distance between the gratings. The particle trajectory is then given by

$$y(z) = \frac{gT^2 z}{L} - \frac{g}{2}\left[\frac{Tz}{L(1+\delta)}\right]^2, \tag{12}$$

and the vertical dispersion at the end of the trajectory is

$$\left.\frac{\mathrm{d}y(z=2L)}{\mathrm{d}\delta}\right|_{\delta=0} = 4gT^2. \tag{13}$$

In Fig. 4, we show the vertical drop and dispersion for a velocity spread $\delta = 0.01$ and a range of particle masses and grating wavelengths.

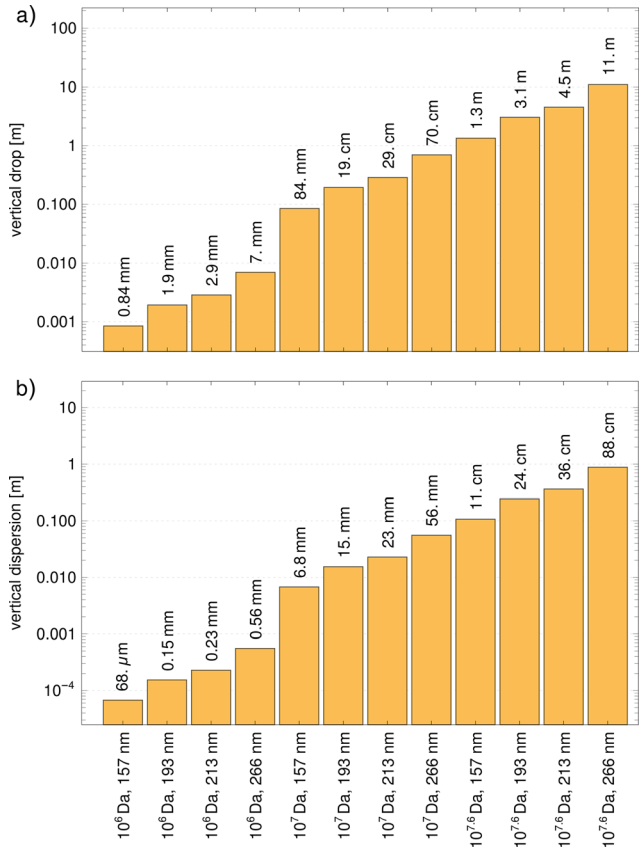

FIG. 4. (a) Height of the particle trajectory in a horizontal beam [Fig. 3(a)] and vertical beam [Figs. 3(b)–3(d), for $\eta = 1$] Talbot–Lau interferometers. (b) Vertical dispersion at the end of a horizontal-beam Talbot–Lau interferometer [Fig. 3(a)]. The labels on the horizontal axis specify the particle mass and the wavelength of the grating laser. The dispersion in a vertical-beam interferometer with transverse pulsed gratings [Fig. 3(c), $\eta = 1$] is smaller by a factor of two. We assume a velocity spread of 1% and a flight time between the gratings $T = .85T_T$. $0.10^{7.6}$ Da $= 40$ MDa is the mass of a tobacco mosaic virus or a 38-nm diameter silicon sphere.

To estimate the dispersion, we use Eq. (13) to make a linear approximation. Figure 4 suggests that a horizontal setup becomes impractical for masses exceeding 10^7 Da, when the vertical drop exceeds tens of centimeters.

The dynamical constraints follow from the dispersion of arrival times at the position of the second and the third grating. In this scheme, the deviations from the desired flight time T are equal for both gratings (i.e., the interferometer remains symmetric for any velocity). The deviations are inversely proportional to the velocity deviation,

$$\left.\frac{1}{T}\frac{\mathrm{d}T_1}{\mathrm{d}\delta}\right|_{\delta=0} = \left.\frac{1}{T}\frac{\mathrm{d}T_2}{\mathrm{d}\delta}\right|_{\delta=0} = -1. \tag{14}$$

The exact tolerance for the deviation of T_1 and T_2 from T depends on n_2 and β, but not on the particle mass. We expect this tolerance to exceed a few percent in most relevant cases and thus the geometric constraints to be more stringent.

08 May 2026 15:38:38

© Author(s) 2022

2. Vertical particle beam, transverse continuous gratings

The vertical analog of the setup discussed above is shown in Fig. 3(b). The total height of such interferometer as well as the relative placement of the gratings depend on the initial vertical component of the particle velocity v_y. We will parametrize the setups using η such that

$$v_y = \eta g T. \tag{15}$$

In this parametrization, $\eta = 0$ corresponds to a setup in which the particles are dropped and $\eta = 1$ describes a symmetric fountain configuration. In the latter, the first and the last grating are at the same y position and the total interferometer height is minimized. For $\eta < 1$ the last grating is located below and for $\eta > 1$ above the first grating. Assuming the first grating is at $y = 0$, the positions y_2 and y_3 of the second and the third gratings are

$$y_2 = \left(\eta - \frac{1}{2}\right) g T^2, \tag{16}$$

$$y_3 = 2(\eta - 1) g T^2, \tag{17}$$

and the peak of the parabolic trajectory is at

$$y_p = \frac{\eta^2 g T^2}{2}. \tag{18}$$

Using the above, we can express the total height of the interferometer as

$$H = \begin{cases} y_3 & \text{for } \eta \geq 2, \\ y_p & \text{for } 2 > \eta \geq 1, \\ y_p - y_3 = (\eta - 2)^2 \dfrac{g T^2}{2} & \text{for } 1 > \eta. \end{cases} \tag{19}$$

For a relative velocity deviation of δ, the arrival time at height y is modified such that

$$\left.\frac{\mathrm{d}t}{\mathrm{d}\delta}\right|_{\delta=0} = \sqrt{\frac{2y_p}{g}}\left(1 \pm \sqrt{\frac{y_p}{y_p - y}}\right), \tag{20}$$

where minus corresponds to the rising and plus to the falling arm of the parabola. Evaluating the above at the positions of the second and the third grating gives

$$\left.\frac{1}{T}\frac{\mathrm{d}T_1}{\mathrm{d}\delta}\right|_{\delta=0} = \eta\left(1 - \frac{\eta}{\eta - 1}\right), \tag{21}$$

$$\left.\frac{1}{T}\frac{\mathrm{d}(T_1 + T_2)}{\mathrm{d}\delta}\right|_{\delta=0} = \eta\left(1 - \frac{\eta}{\eta - 2}\right). \tag{22}$$

Combining the above to estimate $\mathrm{d}s/\mathrm{d}\delta$ and using Eq. (10) with $v = v_y$ allows us to estimate that the beam collimation is subject to a constraint

$$\theta \ll \frac{2\pi\hbar^2}{m^2 d^3 g \tau^2 \eta^2 \delta}\left|1 - \frac{2\eta}{\eta - 1} + \frac{\eta}{\eta - 2}\right|^{-1}. \tag{23}$$

As shown in Fig. 5, for 10^7 Da and $\lambda = 213$ nm the above limitation is stringent, dropping below 10^{-5} rad for launch velocities larger than $\eta = 0.4$ and asymptoting to about 10^{-6} rad. We thus conclude that a continuous-beam vertical scheme with planar gratings is mostly advisable for small launch velocities, such as $\eta = 0.3$. Assuming the latter value, the total height of the interferometer becomes $H \approx 1.4 g T^2$ (see Fig. 6). Given sufficiently tight collimation, such an interferometer configuration could allow for the interference of particles as massive as a tobacco mosaic virus (40 MDa) in a tower with a height of about 10m without using vacuum-UV gratings.[69] If the latter are available, particles with masses up to 10^8 Da could be interfered in a 25 m tower. To relax the collimation requirement of vertical continuous-grating schemes, a pulsed time-domain scheme can be used, which is discussed next.

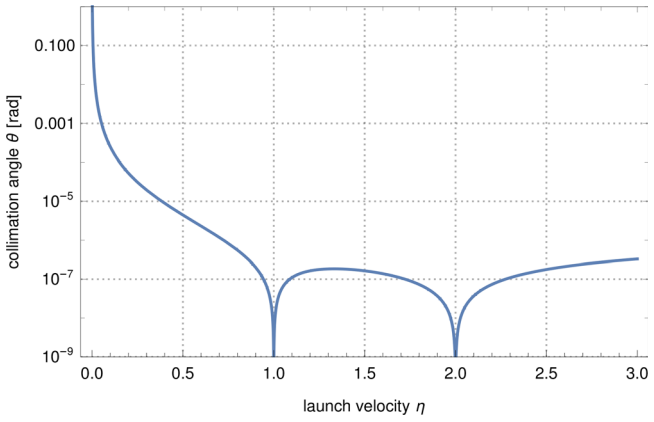

FIG. 5. The upper limit (23) on the molecular beam collimation angle resulting from the timing asymmetry in a vertical-beam continuous transverse-grating Talbot–Lau interferometer [Fig. 3(b)]. We assume a particle mass of 10^7 Da, a grating wavelength of 213 nm, a velocity spread $\delta = 0.01$, and $T = 0.85 T_T$.

3. Vertical particle beam, transverse pulsed gratings

In a pulsed vertical scheme with transverse gratings,[70] similar to the existing OTIMA experiment,[26] the forward velocity acceptance is

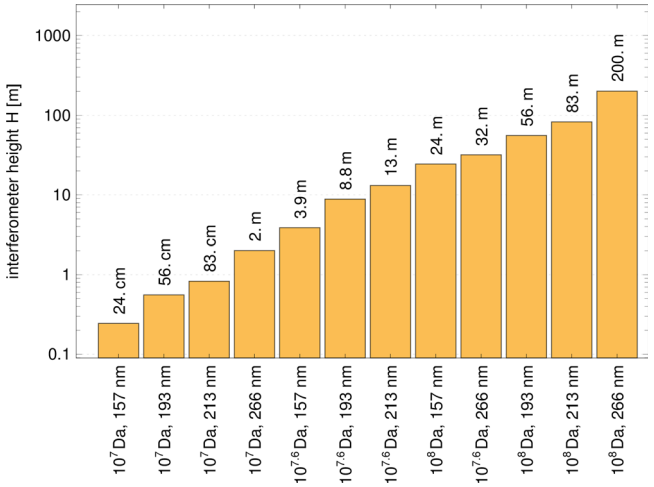

FIG. 6. Total height of the vertical-beam continuous transverse-grating Talbot–Lau interferometer [Fig. 3(b)] for a small launch velocity $v_y = 0.3 g T$ and $T = 0.85 T_T$. The labels on the horizontal axis specify the particle mass and the grating wavelength.

08 May 2026 15:38:38

© Author(s) 2022

limited primarily by the size of the last grating. Assuming the same launch velocity (15) as in the previous scheme, the vertical dispersion of the particles at the time of the third pulse is given as follows:

$$\left.\frac{\mathrm{d}y(t=2T)}{\mathrm{d}\delta}\right|_{\delta=0} = 2\eta g T^2. \tag{24}$$

Equation (24) gives a lower bound on the final vertical extent of the particle cloud. Requiring that the latter is smaller than the vertical size of the grating results in a limit on the forward velocity spread. For a centimeter-sized grating, it amounts to about 1% for 10^7 Da particles, $T = 0.85T_T$, and $\lambda = 213$ nm.

The divergence of the particle beam is limited by the horizontal extent of the gratings and by the need to ensure thin-grating diffraction. The latter is crucial for depletion gratings, for which leaving the thin-grating regime would imply complete transmission loss.[71] For weak gratings, thin-grating diffraction occurs when the collimation angle θ satisfies[60]

$$\theta \ll \frac{\lambda}{vt} = \frac{2h}{\eta\tau mgtd}, \tag{25}$$

where we have taken $v = \eta g T$ corresponding to the forward velocity of the particles at the first grating.[72] For nanosecond pulses, 10^7 Da particles, and a setup with $\lambda = 213$ nm, $\tau = 0.85$, the above limitation is modest, amounting to $\theta \ll 100/\eta$ rad.

4. Vertical particle beam, longitudinal pulsed grating

An arrangement in which the particle beam and the grating are coaxial [as shown in Fig. 3(c)] could potentially have the largest forward velocity acceptance of all the setups considered. That is because the grating fills the entire interferometer and is pulsed, which means that the usual geometrical and dynamical constraints on the velocity spread are either absent or significantly relaxed.

The main difficulty with this scheme is ensuring thin-grating diffraction, which arises because the velocity component of the particles along the grating axis is much larger than in transverse setups. Requiring that

$$t \ll \frac{\lambda}{v}, \tag{26}$$

and inserting v equal to the launch velocity for a symmetric fountain of 10^8 Da particles, $v = gT_T = 13.8\,\mathrm{ms}^{-1}$ for $d = 75$ nm, we find that such a scheme would require single-nanosecond pulses, whose coherence length and spatial extent would be much shorter than the height of the interferometer.

To relax this limitation, one would need to employ a pair of frequency-shifted counterpropagating beams in order to create a standing wave which is comoving with the particles at the time of the grating pulses. In such a setup, for the same mean velocity as above and a spread of 1%, the pulse time would be limited to about 100 ns. The latter is compatible with optical coherence lengths exceeding the fountain height.

D. Particle material

Clusters of metals and dielectrics are highly suitable for high-mass interference experiments due to the relative ease of single-photon ionization, predictable optical properties, precise charge control, and high symmetry. Furthermore, high-flux cluster beams can be reliably produced using magnetron sputtering aggregation sources.[57]

The most important factors to consider when choosing the cluster material are its work function and absorption cross section at the grating wavelength. The former must be smaller than the grating photon energy (typically by at least 0.5 eV) to guarantee efficient ionization upon single photon absorption.[75] The absorption cross section must be high enough to allow for the absorption of $2n_{13} + n_2 \approx 10$ photons in total. Additionally, the β material parameter is important as it affects the total length of the interferometer and the distribution of power between the three gratings.

In Fig. 7, we show the above parameters for a number of materials at the most relevant grating wavelengths. In calculating the values, we use that the absorption cross section of a sub-wavelength sphere is given by

$$\frac{\sigma}{m} = \frac{6\pi}{\lambda\rho}\mathrm{Im}\left\{\frac{\varepsilon-1}{\varepsilon+2}\right\}, \tag{27}$$

where ε and ρ are the electric permittivity and the density of the material, respectively. The polarizability volume is as follows:

$$\frac{\alpha'}{m} = \frac{3}{4\pi\rho}\mathrm{Re}\left\{\frac{\varepsilon-1}{\varepsilon+2}\right\}, \tag{28}$$

and the material constant β^{-1} is then given by Eq. (4).

We find that alkali and alkaline earth metals, such as lithium, calcium, and magnesium, are among the most absorptive at all the wavelengths considered. However, their small density will ultimately make them less suited for high-mass interference, as for large masses the cluster radii will become comparable to the grating wavelength (see Fig. 8). When this happens, the particle absorbs a finite number of photons even at the nodes of the standing waves, which makes the gratings increasingly opaque, suppressing interferometer transmission. We discuss this effect in more detail in Sec. III A.

The above requirements on material density and work function must be satisfied in near-future experiments, but can potentially be bypassed in the long term. In particular, the limitation on the particle size (and thus the density of the material) could be relaxed by implanting the particles with a localized interaction center.[76] The effective work function and absorption cross section could also be modified by coating the clusters or attaching highly absorptive tags.

III. DECOHERENCE MECHANISMS

A. Rayleigh scattering

Rayleigh scattering of grating photons leads to decoherence, because the wavelength of the photons is necessarily comparable to the particle delocalization, and thus, they carry away which-path information. The ratio of probabilities of elastic scattering and of absorption is given by the ratio of the respective cross sections, which for point particles is given by[67]

$$\frac{\sigma_R}{\sigma m} = \frac{\pi^2}{6\rho d^3}\frac{|\varepsilon-1|^2}{\mathrm{Im}\{\varepsilon\}}, \tag{29}$$

where σ_R is the Rayleigh scattering cross section. Since one must typically absorb on the order of 10 photons in an all-optical TLI, Rayleigh scattering can be neglected as long as $\sigma_R/\sigma \ll 0.1$.

08 May 2026 15:38:38

© Author(s) 2022

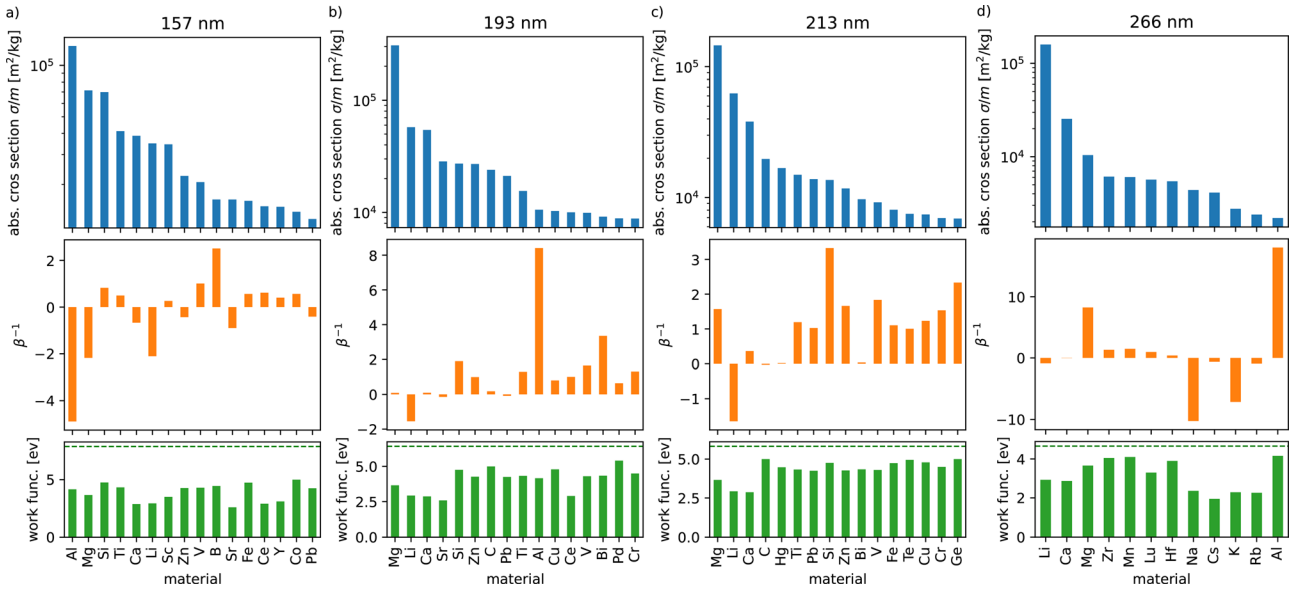
a)
157 nm
b)
193 nm
c)
213 nm
d)
266 nm
abs. cross section σ/m [m²/kg]
β⁻¹
work func. [ev]
material
Al Mg Si Ti Ca Li Sc Zn V B Sr Fe Ce Y Co Pb
Mg Li Ca Sr Si Zn C Pb Tl Al Cu Ce V Bi Pd Cr
Mg Li Ca C Hg Tl Pb Si Zn Bi V Fe Te Cu Cr Ge
Li Ca Mg Zr Mn Lu Hf Na Cs K Rb Al

FIG. 7. Material properties of clusters at the most relevant grating wavelengths (a)–(d). We select the materials for which the electronic and optical properties are found in publicly available databases, and select those for which the work function is 0.5 eV below the photon energy (denoted with a dashed line in the bottom figures). The electric permittivities are sourced from the refractiveindex.info database.[73] The densities and work functions are obtained using the Wolfram language dataset.[74]

B. Collisional decoherence

The visibility loss due to collisional decoherence in a TLI with a total flight time of $2T$ is $R_c = \exp(-2\Gamma_c T)$, where Γ_c is the collision rate. The latter can be estimated from the van der Waals scattering model,[67,77]

$$\Gamma_c \approx \frac{8 p_g}{k_B T_g}\left(\frac{C_6^2 v_g^3}{\hbar^2}\right)^{1/5}, \tag{30}$$

where p_g and T_g are the pressure and temperature of the background gas, and $v_g = \sqrt{2k_B T_g/m_g}$ with m_g the mass of the gas particle. The visibility of the interference pattern decreases due to collisional decoherence to $1/e \approx 37\%$ of its original value when $2\Gamma_c T = 1$, which corresponds to a critical pressure,

$$p_c \approx \frac{1}{\tau m d^2}\left[\frac{(\hbar^2 k_B T_g)^7 m_g^3}{(6\pi C_6)^4}\right]^{\frac{1}{10}}. \tag{31}$$

Note that the critical pressures are lower at lower temperatures; this is because the collision rate is proportional to the density of the gas, which increases with decreasing temperature at a given pressure.

The C_6 coefficient can be calculated directly from the frequency dependence of the complex polarizabilities of the particles or it can be estimated using the London or Slater–Kirkwood formulas.[78] The former reads

$$C_6 \approx \frac{3\bar{\alpha}_g'\bar{\alpha}' U_g U}{2(U_g + U)}, \tag{32}$$

where $\bar{\alpha}_g'$ and $\bar{\alpha}'$ are the static polarizability volumes of the gas and the interfering particle, and U_g and U are their average excitation energies. The Slater–Kirkwood estimate is

$$C_6 \approx \frac{3}{2}\frac{e\hbar}{\sqrt{4\pi\varepsilon_0 m_e}}\frac{\bar{\alpha}_g'\bar{\alpha}'}{\sqrt{\bar{\alpha}_g'/N_g} + \sqrt{\bar{\alpha}'/N}}, \tag{33}$$

where e, m_e are the charge and mass of the electron, and N_g, N are the number of valence electrons in the gas and in the interfering particle. The two formulas both essentially implement the Unsöld approximation[78] and thus yield similar results.

In Table I, we show the critical pressures obtained for clusters of hafnium as a representative example. We use the Slater–Kirkwood formula and take the static polarizability of the cluster to be $\alpha' = r^3$, that is, the static polarizability of a conducting sphere. We use $\alpha_g' = 1.74\,\text{Å}^3$, $N_g = 10$ for molecular nitrogen and $\alpha_g' = 0.80\,\text{Å}^3$, $N_g = 2$ for hydrogen.[79] For the clusters, we assume four valence electrons per atom, corresponding to the hafnium's preferred oxidation state.

C. Thermal decoherence

In a TLI with a total flight time of $2T$, the visibility reduction R_{th} due to absorption and emission of thermal photons is given as follows:[67]

$$\log R_{\text{th}} = -2Tc\int_0^\infty \mathrm{d}k\,[\gamma_{\text{abs}}(k) + \gamma_{\text{emi}}(k)]\left[1 - \frac{1}{kd\tau}\text{Si}(kd\tau)\right], \tag{34}$$

where $\gamma_{\text{abs}}(k)$ and $\gamma_{\text{emi}}(k)$ are the spectral emission and absorption rates, respectively, and *Si* is the sine integral.

In Eq. (34), the emission and absorption rates are weighted with a decoherence kernel expressing the amount of which-path information carried away by a photon of a given wavelength. The kernel is plotted in Fig. 9 as a function of the dimensionless ratio kd for $\tau = 1$. From the plot, we see that the decoherence kernel has a relatively simple dependence on kd, which can be approximated as follows:

08 May 2026 15:38:38

© Author(s) 2022

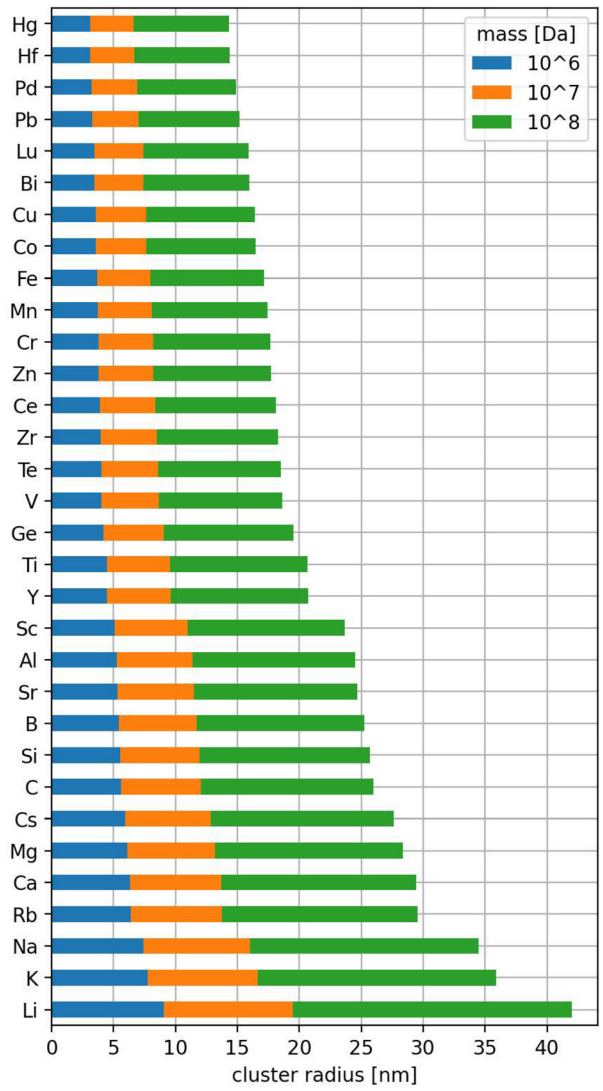

Fig. 8. Cluster radius as a function of material and mass. Data sources as in Fig. 7.

$$\left[1-\frac{1}{kd\tau}\mathrm{Si}(kd\tau)\right]\approx\begin{cases}\dfrac{(kd\tau)^2}{18} & kd\le 3/\tau,\\ 1-\dfrac{\pi}{2kd\tau} & kd>3/\tau.\end{cases}\tag{35}$$

Using the above algebraic approximation allows us to give a closed-form expression for the visibility reduction R_{th} in many cases.

For the sources we consider, we can approximate the internal cluster temperature as equal to the temperature of the environment. This means that the photon emission and absorption rates will be equal, $\gamma_{\mathrm{abs}}(k)=\gamma_{\mathrm{emi}}(k)=\gamma(k)$. They can be modeled as Planck spectra modified by the spectral emissivity of the particle, which is proportional to its absorption cross section,

$$\gamma(k)=\frac{\sigma(k)k^2}{\pi^2[\exp(\hbar kc/k_BT_e)-1]}.\tag{36}$$

Table I. Critical pressures for collisional decoherence of hafnium clusters with N_2 or H_2 background gas. We assume a grating wavelength of 266 nm and $\tau=0.85$.

	$p_c^{N_2}$ [mbar]		$p_c^{H_2}$ [mbar]	
m [Da]	300 K	80 K	300 K	80 K
10^5	2×10^{-7}	7×10^{-8}	1×10^{-7}	5×10^{-8}
10^6	8×10^{-9}	3×10^{-9}	5×10^{-9}	2×10^{-9}
10^7	3×10^{-10}	1×10^{-10}	2×10^{-10}	8×10^{-11}
10^8	1×10^{-11}	5×10^{-12}	8×10^{-12}	3×10^{-12}

Equation (36) neglects corrections resulting from the finite heat capacity of the cluster.[80] Other modifications of the radiation law discussed in Ref. 81 also do not apply in our case. In particular, our clusters are thermalized with the seed gas, so they form a canonical ensemble rather than a microcanonical one. Furthermore, our clusters are immersed in an equally hot thermal radiation of the interferometer chamber, so stimulated emission can occur. Finally, it is convenient to rewrite the emission and absorption rates as a product of two factors,

$$\gamma(k)=\underbrace{\frac{\sigma(k)}{\pi^2d^2}}_{\text{cross section}}\underbrace{\frac{(kd)^2}{\exp(\beta_ekd)-1}}_{\text{Planck}},\tag{37}$$

where $\beta_e=\hbar c/dk_BT_e$ is the dimensionless inverse temperature. The Planck factor is shown in Fig. 9 for $T_e=300$ K and $d=133$ nm, which corresponds to $\beta_e\approx53$. We see that the Planck term will effectively limit the integration in Eq. (34) to $kd<0.3$, which corresponds to wavelengths greater than 2.8 μm or photon energies smaller than 0.45 eV. Restriction to such long wavelengths will allow us to use the small-argument approximation Eq. (35) of the kernel.

For many metals, the electric permittivity necessary to calculate the absorption cross section of the cluster is not known for such long wavelengths and must be modeled. We will use that, for most metals, ε can be approximated reasonably well by a sum of two contributions, arising from free and from bound electrons.[83] The latter term is mostly important in the region where $|\mathrm{Re}\{\varepsilon\}|$ is small, which for hafnium is roughly above 0.5 eV.[84] Below this energy, it contributes a bounded

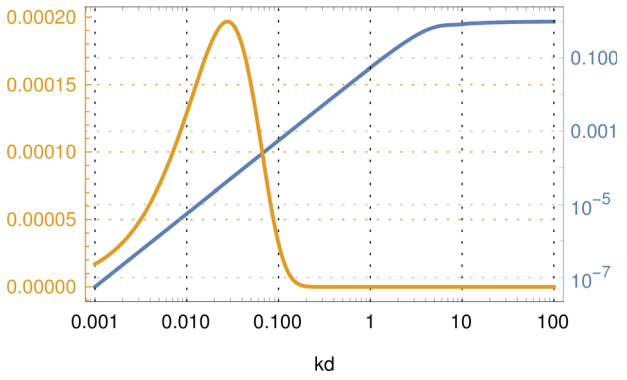

Fig. 9. Terms contributing to the thermal decoherence rate: the Planck factor [orange, see Eq. (37)] and the decoherence kernel [blue, Eq. (35)]. We take $\tau=1$, a temperature of 300 K, and a grating period $d=133$ nm.

08 May 2026 15:38:38

© Author(s) 2022

real value of the order of unity,[83] which we will neglect. This leaves us with the Drude term,[85]

$$\varepsilon(\omega) = 1 - \frac{\omega_P^2}{\omega(\omega + \imath\gamma_P)}, \tag{38}$$

in which ω_P and γ_P are the plasma frequency and damping constant, respectively. Inserting the above into the absorption cross section of a sub-wavelength sphere, Eq. (27), gives the cross section shown in Fig. 10. In the IR limit relevant to us ($kd < 0.3$), the cross section can be approximated by a power law,

$$\frac{\sigma(kd)}{\pi^2 d^2} \approx \frac{9mc\gamma_P}{\pi\rho d^4 \omega_P^2} kd. \tag{39}$$

Inserting the approximate kernel (35) and the emission rate (37) with the approximate absorption cross section (39) into Eq. (34) gives

$$\log R_{\text{th}} \approx -\frac{\tau^3 m^2 c^2 \gamma_P}{\hbar\pi^2 \rho d^3 \omega_P^2} \int_0^\infty \mathrm{d}(kd)\, \frac{(kd)^5}{\exp(\beta_e kd) - 1} = \frac{8\pi^4 \tau^3 m^2 c^2 \gamma_P}{63\hbar\rho d^3 \omega_P^2 \beta_e^6}. \tag{40}$$

To observe interference, we must have $\log R_{\text{th}} < 1$, from which we obtain the maximum permissible temperature T_e of the clusters and the chamber,

$$T_e = \left(\frac{63\hbar^7 c^4 \rho \omega_P^2}{8\pi^4 \tau^3 m^2 \gamma_P d^3 k_B^6} \right)^{\frac{1}{6}}. \tag{41}$$

To calculate the critical temperature, we first estimate the plasma frequency ω_P as the free-electron value,

$$\omega_P = \sqrt{\frac{n_e e^2}{m_e \varepsilon_0}}, \tag{42}$$

in which n_e is the electron number density and m_e is the electron mass. The former is easily obtained from bulk material density ρ, the number of valence electrons N, and the atomic mass. To estimate the damping constant γ_P, we first estimate the bulk value using DC electrical resistivity[86] ρ_{DC} at 300 K, via[87]

$$\gamma_P^{\text{bulk}} = \frac{n_e e^2 \rho_{DC}}{m_e}. \tag{43}$$

We then apply the mean-free path correction,[82]

$$\gamma_P = \gamma_P^{\text{bulk}} + \frac{4}{3}\frac{v_F}{r}, \tag{44}$$

where v_F is the Fermi velocity, obtained from the Fermi energy E_F as[87]

$$v_F = \sqrt{\frac{2E_F}{m_e}}, \quad E_F = \frac{\hbar^2}{2m_e}(3\pi^2 n_e)^{\frac{2}{3}}. \tag{45}$$

The relative magnitude of the correction (44) for hafnium clusters is about 100% for 10^5 Da and decays to about 10% for 10^8 Da. The critical temperatures obtained using the above approach are given in Table II.

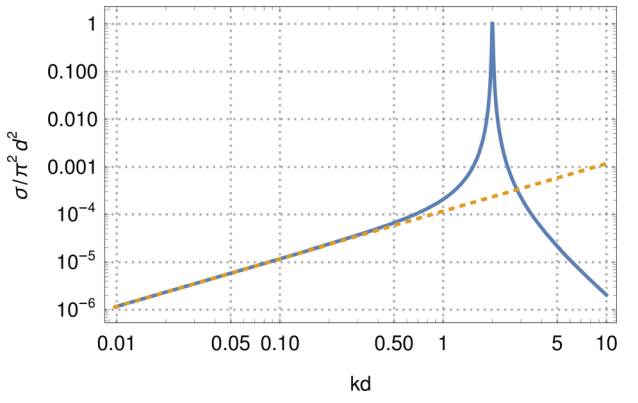

FIG. 10. Absorption cross section of hafnium clusters in units of $\pi^2 d^2$ calculated using the full Drude model (38) (blue) and using the power-law approximation (39) (orange, dotted). Plotted for $\omega_P = 1.0 \times 10^{17}\ \text{s}^{-1}$ and $\gamma = 4.5 \times 10^{15}\ \text{s}^{-1}$ and $m = 10^8$ Da. The pronounced cusp is the surface plasmon resonance.[82]

IV. ROADMAP TO UNIVERSAL HIGH-MASS INTERFERENCE

The above discussion allows us to sketch a plausible roadmap to matter wave interference up to four orders of magnitude in mass beyond the current record of 2.7×10^4 Da. As a first step, we envisage an update of the LUMI experiment (LUMI 2.0) to a configuration with three optical ionizing gratings with a wavelength of 266 nm [retaining the horizontal configuration, as in Fig. 3(a)]. This setup should allow for the interference of clusters up to 10^6 Da with a limited free fall of about 1 cm (see Fig. 4). The photon energy of 4.7 eV will allow us to use clusters of metals which sputter abundantly and are easily ionizable, such as yttrium (see Fig. 7). Beyond this, we propose a further upgrade of LUMI to gratings with a wavelength below 220 nm (LUMI 2.5). The increased photon energy will increase the ionization efficiency and thus substantially expand the class of compatible materials to include dielectrics, such as silicon. Additionally, the smaller grating period will open up the possibility of interfering particles a few MDa in mass.

Vertical fountain configurations can pave the way to even higher masses, provided advanced cooling schemes can achieve the required small launch velocities. A fountain with transverse pulsed gratings [Fig. 3(c)] avoids the stringent collimation requirements (and the

TABLE II. Material properties used for and the result of the estimation of the Drude model parameters: the plasma frequency ω_P and the damping constant γ_P.

	n_e [cm^{-3}]	ρ_{DC} [Ω m]	ω_P [s^{-1}]	γ_P^{bulk} [s^{-1}]
Hf	1.8×10^{23}[a]	3.4×10^{-7}[b]	2.4×10^{16}	1.7×10^{15}
Li	4.6×10^{22}	9.5×10^{-8}[b]	1.22×10^{16}	1.2×10^{14}

	T_e (K)			
	10^5 Da	10^6 Da	10^7 Da	10^8 Da
Hf	950	460	220	100
Li	520	270	140	70

[a]Assuming four valence electrons per hafnium atom.
[b]See Ref. 79.

08 May 2026 15:38:38

© Author(s) 2022

resulting limitation on launch velocity, see Fig. 5) of a vertical continuous-grating scheme [Fig. 3(b)]. A first interferometer of this type could be realized as a 70-cm-tall symmetric fountain ($\eta = 1$) with three 266-nm gratings, which would bring the interference of 10^7 Da particles within reach (see Fig. 4). The use of nanosecond pulse lengths would ensure very lenient beam collimation requirements. The final grating would require a vertical extent of 6 cm to fully accommodate the spread of the beam (see Fig. 4). Here, we note that the fundamental velocity selectivity of a pulsed scheme limits the signal of a source with a wide forward velocity spread, which may restrict compatible beam sources or require advanced beam cooling techniques.

We expect that cooling of the particles and of the apparatus to liquid-nitrogen temperatures will be necessary to observe the interference of particles with a mass of 10^7 Da or larger (see Table II). In cluster sources, the necessary particle temperature can be achieved through thermalization of the clusters with a cryogenic seed gas. For cooling of the apparatus, a copper shield connected to a liquid nitrogen bath should be sufficient. Thanks to the relatively compact size of the proposed fountain setup, the overall cooling requirements will likely be less severe than what has already been achieved in successful antimatter experiments.[88]

Lengthening the 70-cm transverse-pulsed-grating fountain by an order of magnitude would yield an experiment potentially suitable for the interference of a tobacco mosaic virus ($m = 4 \times 10^7$ Da) or for the interference of 10^8 Da particles. The former would require a fountain 5 m in height (assuming 213 nm gratings), while the latter would require a height of 8 m (assuming 157 nm gratings), which is comparable with present-day atom interferometers. We consider here only symmetric schemes ($\eta = 1$) to take full advantage of the available height. A formidable experimental challenge for such tall fountains is the dispersion of the beam at the position of the third grating: 36 and 68 cm for 1% velocity spread in the 5 and 8 m schemes, respectively. To avoid dephasing, the mirror must have a surface roughness much less than the grating period d over the vertical extent of the gratings.

Finally, the coaxial scheme illustrated in Fig. 3(d) could potentially have many benefits, at the cost of a significantly increased experimental overhead. For the interference of 10^8 Da particles, the scheme would require well-timed Fourier-limited pulses of high power and 10 m coherence length in the deep ultraviolet (below 200 nm). Additionally, the wavefronts would have to be well defined over long distances and the beam source would have to be cold and intense.

The above roadmap is built on conservative assumptions regarding existing and future laser technology. The first stages (LUMI 2.0 and the 70 cm fountain) use radiation at 266 nm, which is readily obtained as the fourth harmonic of a Nd:YAG laser and available at high powers and repetition rates. The subsequent stages employ wavelengths around 213 nm, at which highly coherent beams with powers well beyond 100 mW (Ref. 89) are available via frequency quadrupling of intense Ti:sapphire laser light, and nanosecond pulses of several millijoules can be prepared by quintupling the radiation from a solid-state or fiber laser. Only for the most ambitious schemes do we propose using radiation below 190 nm. Because of the limited coherence length at this wavelength, a transverse-grating design may be favorable, and we note the challenges resulting from the attenuation of radiation below 190 nm in air. The necessity of guiding light in evacuated or purged pipes might favor interferometers in the capsules of drop towers as opposed to long beam lines in tall fountains. Finally, depending on the choice of the particle material, certain specific wavelengths different from the ones proposed may be advised. Solid state optical parametric oscillators and dye lasers can provide this flexibility, at the expense of somewhat reduced average power.

V. CONCLUSION

A recent series of impressive experiments and ambitious proposals are bringing quantum mechanics to an increasingly macroscopic realm. The rapid progress in quantum control of levitated nanoparticles[90] and a growing number of proposals for probing quantum gravity[34,91] illustrate the surging interest in macroscopic quantum physics. Mass, spatial delocalization extent, and the number of constituent particles are just some of the many criteria suggested for quantifying the macroscopicity a quantum state.[92] Regardless of the precise criteria used, demonstrating center-of-mass interference of increasingly massive particles is significant as it robustly rules out the parameter space of proposed modifications to linear quantum mechanics.[37] The experiments we propose will also create large spatial delocalizations—typically an order of magnitude larger than the particle diameter—and coherence times on the order of one second.

While there is no experimental indication as of yet that quantum mechanics fails beyond a certain regime, there is good justification for believing that our current picture of the world is incomplete. The tension between quantum mechanics and general relativity is one such hint, which inspired Roger Penrose and others to study models in which gravity itself can lead to wavefunction collapse. We anticipate that, in the short term, upgrades to an existing experiment will enable interference of 10^6 Da metal clusters and have outlined a roadmap toward interferometry with particles as large as 10^8 Da. With such experiments, quantum mechanics is undoubtedly entering the realm of the macroscopic; whether the theory will withstand these ever more demanding tests is an open and very exciting question.

ACKNOWLEDGMENTS

We thank the Austrian Science Fund (FWF) for support in Project No. P32543-N as well as the Gordon and Betty Moore Foundation for support within Project No. 10771. We thank Philipp Geyer for continuous experimental support, Armin Shayeghi for many stimulating discussions on cluster science and matter-wave interferometry, and Bernd von Issendorff for his advice on cluster physics. We acknowledge fruitful collaboration throughout the years with Stefan Nimmrichter, Klaus Hornberger, Ben Stickler, and Stefan Kuhn.

AUTHOR DECLARATIONS

Conflict of Interest

The authors have no conflicts to disclose.

DATA AVAILABILITY

The data that support the findings of this study are available from the corresponding author upon reasonable request.

APPENDIX: OPTICAL DEPLETION GRATINGS BEYOND THE POINT PARTICLE APPROXIMATION

For a point-like particle, the mean number of photons absorbed as a function of position in the grating is as follows:

08 May 2026 15:38:38

© Author(s) 2022

$$\bar{n}(x) = \frac{n_0}{2}\left[1 + \cos\left(\frac{2\pi x}{d}\right)\right], \tag{A1}$$

where n_0 is the mean number of photons absorbed at the antinodes. For a particle with a finite size, the mean number of absorbed photons becomes[67]

$$\bar{n}(x) = n_+ + n_- \cos\left(\frac{2\pi x}{d}\right), \tag{A2}$$

where $n_- < n_+$. The latter means that the particle absorbs a finite number of photons even at the nodes, which gradually renders the depletion gratings opaque as the size of the particle increases.

Specifically, as the size of the particle is increased, the modulation n_- must be kept finite in order to maintain a good signal visibility. For $T = T_T$, the latter is given by[67]

$$V_{T=T_T} = \frac{2I_1^2(n_-)I_2(n_-)}{I_0^3(n_-)}, \tag{A3}$$

where for simplicity we have assumed three identical gratings. Equation (A3) implies that maintaining $V_{T=T_T} = 50\%$ requires keeping $n_- = 2.6$. The ratio of n_+ and n_- is given by the ratio of Mie absorption coefficients $\Pi^{\pm}_{\text{abs}}$ and depends on the size of the cluster and on the material, but not on the laser intensity.[67] The ratio

$$\frac{n_+}{n_-} = \frac{\Pi^+_{\text{abs}}}{\Pi^-_{\text{abs}}} \tag{A4}$$

can be calculated numerically, yielding the size-dependence of n_+ and thus of the interferometer transmission via

$$t = \exp(-3n_+) I_0^3(n_-). \tag{A5}$$

The resulting transmission is shown for hafnium and sillicon clusters with $\lambda = 150$ nm in Figs. Fig. 11(a) and 12(a).

To calculate the dependence of laser intensity on particle size, we use that for a time-domain setup with pulse energy E_L and area a_L, we have[93]

$$n_\pm = \frac{2\pi\Pi^{(\pm)}_{\text{abs}} E_L}{\hbar c k^3 a_L}. \tag{A6}$$

The laser intensity required for a given $V_{T=T_T}$ can thus be obtained by calculating Π^-_{abs} numerically. An example dependence for hafnium and sillicon clusters with $\lambda = 150$ nm is shown in Figs. 11(b) and 12(b).

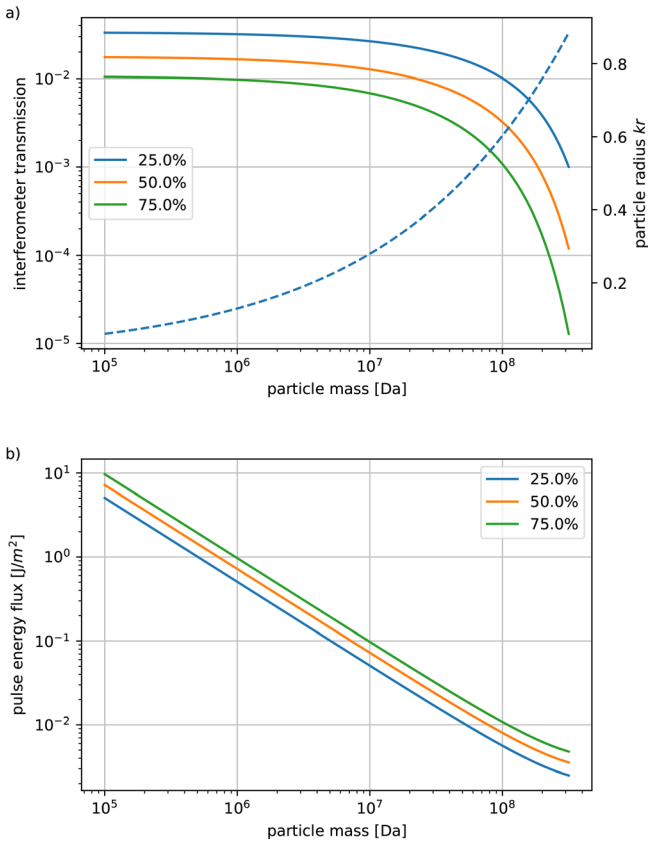

Fig. 11. (a) Mean transmission of a TLI for hafnium clusters with depletion gratings with a wavelength of 150 nm. Different continuous curves correspond to different values of visibility, see Eq. (A3). The mean number of absorbed photons is taken to be equal for all three gratings. The dashed line shows the dimensionless particle radius *kr*. (b) Grating pulse energy flux as function of mass for hafnium clusters and a grating with a wavelength of 150 nm.

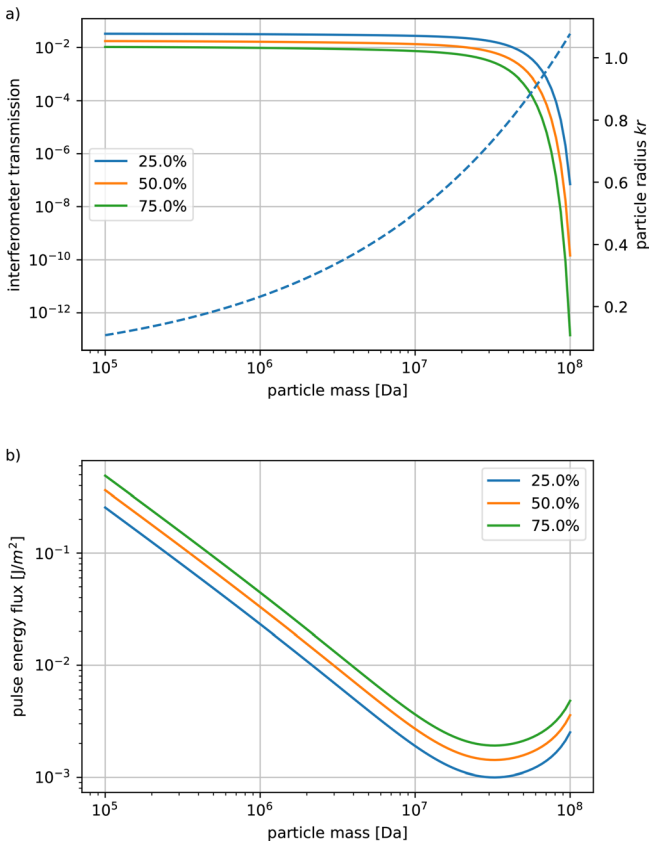

Fig. 12. As in Fig. 11, but for clusters of silicon.

08 May 2026 15:38:38

© Author(s) 2022

REFERENCES

[1]L. De Broglie, Nature **112**, 540 (1923).
[2]E. Schrödinger, Ann. Phys. **79**, 361 (1926).
[3]C. Davisson and L. H. Germer, Phys. Rev. **30**, 705 (1927).
[4]G. P. Thomson and A. Reid, Nature **119**, 890 (1927).
[5]I. Estermann and O. Stern, Z. Phys. **61**, 95 (1930).
[6]H. von Halban and P. Preiswerk, C. R. Acad. Sci. Paris **203**, 73 (1936).
[7]P. E. Moskowitz, P. L. Gould, S. R. Atlas, and D. E. Pritchard, Phys. Rev. Lett. **51**, 370 (1983).
[8]P. L. Gould, G. A. Ruff, and D. E. Pritchard, Phys. Rev. Lett. **56**, 827 (1986).
[9]D. W. Keith, M. L. Schattenburg, H. I. Smith, and D. E. Pritchard, Phys. Rev. Lett. **61**, 1580 (1988).
[10]O. Carnal, A. Faulstich, and J. Mlynek, Appl. Phys. B **53**, 88 (1991).
[11]C. Bordé, N. Courtier, F. D. Burck, A. Goncharov, and M. Gorlicki, Phys. Lett. A **188**, 187 (1994).
[12]M. Kasevich and S. Chu, Phys. Rev. Lett. **67**, 181 (1991).
[13]D. W. Keith, C. R. Ekstrom, Q. A. Turchette, and D. E. Pritchard, Phys. Rev. Lett. **66**, 2693 (1991).
[14]A. D. Cronin, J. Schmiedmayer, and D. E. Pritchard, Rev. Mod. Phys. **81**, 1051 (2009).
[15]G. Tino and M. Kasevich, in *Proceedings of the International School of Physics Enrico Fermi* (IOS, Varenna, 2014), Vol. 188.
[16]P. Asenbaum, C. Overstreet, M. Kim, J. Curti, and M. A. Kasevich, Phys. Rev. Lett. **125**, 191101 (2020).
[17]L. Zhou *et al.*, Phys. Rev. A **104**, 022822 (2021).
[18]Y. A. El-Neaj *et al.*, EPJ Quantum Technol. **7**, 6 (2020).
[19]C. Burrage, A. Kuribayashi-Coleman, J. Stevenson, and B. Thrussell, J. Cosmol. Astropart. Phys. **2016**, 041.
[20]P. Hamilton, M. Jaffe, P. Haslinger, Q. Simmons, H. Müller, and J. Khoury, Science **349**, 849 (2015).
[21]G. Rosi, F. Sorrentino, L. Cacciapuoti, M. Prevedelli, and G. M. Tino, Nature **510**, 518 (2014).
[22]L. Morel, Z. Yao, P. Clade, and S. Guellati-Khelifa, Nature **588**, 61 (2020).
[23]M. Arndt, O. Nairz, J. Voss-Andreae, C. Keller, G. van der Zouw, and A. Zeilinger, Nature **401**, 680 (1999).
[24]B. Brezger, L. Hackermüller, S. Uttenthaler, J. Petschinka, M. Arndt, and A. Zeilinger, Phys. Rev. Lett. **88**, 100404 (2002).
[25]S. Gerlich *et al.*, Nat. Phys. **3**, 711 (2007).
[26]P. Haslinger, N. Dorre, P. Geyer, J. Rodewald, S. Nimmrichter, and M. Arndt, Nat. Phys. **9**, 144 (2013).
[27]Y. Y. Fein, P. Geyer, P. Zwick, F. Kiałka, S. Pedalino, M. Mayor, S. Gerlich, and M. Arndt, Nat. Phys. **15**, 1242 (2019).
[28]T. Kovachy, P. Asenbaum, C. Overstreet, C. A. Donnelly, S. M. Dickerson, A. Sugarbaker, J. M. Hogan, and M. A. Kasevich, Nature **528**, 530 (2015).
[29]C. Whittle *et al.*, Science **372**, 1333 (2021).
[30]U. Delić, M. Reisenbauer, K. Dare, D. Grass, V. Vuletić, N. Kiesel, and M. Aspelmeyer, Science **367**, 892 (2020).
[31]L. Magrini, P. Rosenzweig, C. Bach, A. D.-O. Sebastian, G. Hofer, S. Hong, N. Kiesel, A. Kugi, and M. Aspelmeyer, arXiv:2012.15188v1 (2020).
[32]F. Tebbenjohanns, M. L. Mattana, M. Rossi, M. Frimmer, and L. Novotny, Nature **595**, 378 (2021).
[33]O. Romero-Isart, L. Clemente, C. Navau, A. Sanchez, and J. I. Cirac, Phys. Rev. Lett. **109**, 147205 (2012).
[34]S. Bose *et al.*, Phys. Rev. Lett. **119**, 240401 (2017).
[35]B. A. Stickler, B. Papendell, S. Kuhn, B. Schrinski, J. Millen, M. Arndt, and K. Hornberger, New J. Phys. **20**, 122001 (2018).
[36]B. Schrinski, B. A. Stickler, and K. Hornberger, J. Opt. Soc. Am. B **34**, C1 (2017).
[37]S. Nimmrichter and K. Hornberger, Phys. Rev. Lett. **110**, 160403 (2013).
[38]B. Schrinski, S. Nimmrichter, B. A. Stickler, and K. Hornberger, Phys. Rev. A **100**, 032111 (2019).
[39]R. Penrose, Gen. Relativ. Gravitation **28**, 581 (1996).
[40]G. C. Ghirardi, A. Rimini, and T. Weber, Phys. Rev. D **34**, 470 (1986).
[41]P. Pearle, Phys. Rev. A **39**, 2277 (1989).
[42]L. Diosi, Phys. Lett. A **105**, 199 (1984).
[43]D. Giulini and A. Großardt, Classical Quantum Gravity **30**, 155018 (2013).
[44]I. C. Percival and W. T. Strunz, Proc. R. Soc. London, Ser. A **435**, 431 (1997).
[45]C. H. T. Wang, R. Bingham, and J. T. Mendonça, Classical Quantum Gravity **23**, L59 (2006).
[46]M. Zych, F. Costa, I. Pikovski, and C. Brukner, Nat. Commun. **2**, 505 (2011).
[47]I. Pikovski, M. Zych, F. Costa, and C. Brukner, Nat. Phys. **11**, 668 (2015).
[48]M. Toroš, G. Gasbarri, and A. Bassi, Phys. Lett. A **381**, 3921 (2017).
[49]W. H. F. Talbot, Philos. Mag. **9**, 401 (1836).
[50]E. Lau, Ann. Phys. **6**, 417 (1948).
[51]J. F. Clauser and S. Li, Phys. Rev. A **49**, R2213 (1994).
[52]J. Clauser, "De Broglie-wave interference of small rocks and live viruses," in *Experimental Metaphysics*, edited by R. S. Cohen, M. Horne, and J. Stachel (Kluwer Academic, Dordrecht, 1997), pp. 1–11.
[53]Y. Fein, A. Shayeghi, L. Mairhofer, F. Kiałka, P. Rieser, P. Geyer, S. Gerlich, and M. Arndt, Phys. Rev. X **10**, 011014 (2020).
[54]Y. Y. Fein, P. Geyer, F. Kiałka, S. Gerlich, and M. Arndt, Phys. Rev. Res. **1**, 033158 (2019).
[55]Y. Y. Fein, A. Shayeghi, F. Kialka, P. Geyer, S. Gerlich, and M. Arndt, Phys. Chem. Chem. Phys. **22**, 14036 (2020).
[56]J. Schätti, V. Köhler, M. Mayor, Y. Y. Fein, P. Geyer, L. Mairhofer, S. Gerlich, and M. Arndt, J. Mass Spectrom. **55**, e4514 (2020).
[57]H. Haberland, M. Karrais, and M. Mall, Z. Phys. D **20**, 413 (1991).
[58]T. Juffmann, S. Truppe, P. Geyer, A. G. Major, S. Deachapunya, H. Ulbricht, and M. Arndt, Phys. Rev. Lett. **103**, 263601 (2009).
[59]J. Bateman, S. Nimmrichter, K. Hornberger, and H. Ulbricht, Nat. Commun. **5**, 4788 (2014).
[60]F. Kiałka, "Talbot–Lau schemes and Bragg diffraction: Theory and applications in high-mass matter-wave interferometry," Ph.D. thesis (University of Vienna, University of Duisburg-Essen, 2021).
[61]F. Kiałka, B. A. Stickler, K. Hornberger, Y. Y. Fein, P. Geyer, L. Mairhofer, S. Gerlich, and M. Arndt, Phys. Scr. **94**, 034001 (2019).
[62]C. Brand *et al.*, Nat. Nanotechnol. **10**, 845 (2015).
[63]Y. Y. Fein, "Long-baseline universal matter-wave interferometry," Ph.D. thesis (University of Vienna, 2020).
[64]J. Schätti, M. Kriegleder, M. Debiossac, M. Kerschbaum, P. Geyer, M. Mayor, M. Arndt, and V. Köhler, Chem. Commun. **55**, 12507 (2019).
[65]N. Dörre, J. Rodewald, P. Geyer, B. von Issendorff, P. Haslinger, and M. Arndt, Phys. Rev. Lett. **113**, 233001 (2014).
[66]Most importantly, the grating wavelengths must be commensurate and the distances between the gratings must be such that semiclassical trajectories form a closed interferometer (Ref. 60). In the most straightforward configuration combining transmission and phase gratings, the period of the latter is twice the period of the depletion grating. Compared to a triple-transmission setup, such a configuration would offer increased particle flux, but reduced visibility and no advantage in total duration.
[67]S. Nimmrichter, "Macroscopic matter-wave interferometry," Ph.D. thesis (University of Vienna, 2013).
[68]For a finite number of absorbed photons n, small values of β imply a diverging phase modulation and are therefore not physical.
[69]Interferometry with viruses in such a scheme would likely require decorating them with photoionizable tags to achieve ionization-based transmission gratings at the considered wavelengths.
[70]E. Reiger, L. Hackermueller, M. Berninger, and M. Arndt, Opt. Commun. **264**, 326 (2006).
[71]For a phase grating, leaving the thin-grating regime would mean that the populations of the diffraction orders depend on the forward velocity and are not symmetric around the zeroth order. However, this should not wash out the Talbot pattern, as the emergence of the latter depends on the equal separation of the diffraction orders in momentum space and not on their magnitudes.
[72]For $\eta < 1$ the forward velocity at the third grating is larger and must be used instead.
[73]M. N. Polyanskiy, see https://refractiveindex.info for "Refractive Index Database."
[74]See https://reference.wolfram.com/language/note/ElementDataSourceInformation.html.
[75]For simplicity, we neglect here the finite-size effects, which can be included to a first approximation using the empirical formula for the ionization potential, Ref. 94 $I = W + 3e^2/(32\pi\epsilon_0 r)$, where W is the work function and r is the

08 May 2026 15:38:38

© Author(s) 2022

radius of the cluster. For high-density materials, such as hafnium, the correction amounts to a few tenths of an electronvolt for 10^5 Da clusters.
[76]M. Scala, M. S. Kim, G. W. Morley, P. F. Barker, and S. Bose, Phys. Rev. Lett. **111**, 180403 (2013).
[77]K. Hornberger, J. E. Sipe, and M. Arndt, Phys. Rev. A **70**, 053608 (2004).
[78]A. Stone, *The Theory of Intermolecular Forces* (Oxford University, Oxford, 2013).
[79]*CRC Handbook of Chemistry and Physics*, 97th ed., edited by W. Haynes, D. R. Lide, and T. J. Bruno (CRC, London, 2016).
[80]This is justified for clusters consisting of more than 1000 atoms, which store more than 10 eV of internal energy even at 80 K. The most probable emission for such clusters would be in the far infrared (beyond 10 μm), and thus more than 100 photons would have to be emitted before the internal temperature changes by more than 10%.
[81]K. Hansen and E. E. B. Campbell, Phys. Rev. E **58**, 5477 (1998).
[82]U. Kreibig and M. Vollmer, *Optical Properties of Metal Clusters*, Springer Series in Materials Science Vol. 25 (Springer, New York, 1995).
[83]C. F. Bohren and D. R. Huffman, *Absorption and Scattering of Light by Small Particles* (Wiley, New York, 1983).
[84]D. W. Lynch, C. G. Olson, and J. H. Weaver, Phys. Rev. B **11**, 3617 (1975).
[85]In some previous treatments of thermal decoherence in a TLI, the short-wavelength limit of the Drude expression has been used instead Ref. 67, $\varepsilon(\omega) = 1 - \omega_P^2/\omega^2 + \imath\gamma\omega_P^2/\omega^3 + O(1/\omega^4)$. In our case, the Planck term limits the integration in (34) to wavelengths for which the above approximation fails. It is, therefore, important to insert the full Drude expression (38) into (27).
[86]The damping constant could also be obtained from measured low-energy absorptivity $A = 2\gamma_P^{\text{bulk}}/\omega_P$, as in Ref. 84. However, the absorptivity is often measured in temperatures much lower than that of the clusters, which could lead to significant errors as the dependence of γ_P^{bulk} on temperature is strong (Ref. 87). Finally, one could also obtain the Drude parameters by fitting measured complex permittivities using (38). However, measured permittivity data typically rely on a free-electron Drude extrapolation in the low-frequency regime to facilitate the Kramers–Kroenig analysis. As a result, there is no benefit to fitting the permittivity over using the low-frequency absorptivity directly.
[87]N. Ashcroft and N. D. Mermin, *Solid State Physics* (Harcourt College, Fort Worth, 1976).
[88]M. Ahmadi *et al.*, Nature **557**, 71 (2018).
[89]Y. Kaneda, T. Tago, T. Sasa, M. Sasaura, H. Nakao, J. Hirohashi, and Y. Furukawa, Opt. Express **27**, 8021 (2019).
[90]C. Gonzalez-Ballestero, M. Aspelmeyer, L. Novotny, R. Quidant, and O. Romero-Isart, Science **374**, eabg3027 (2021).
[91]C. Marletto and V. Vedral, Phys. Rev. Lett. **119**, 240402 (2017).
[92]F. Fröwis, P. Sekatski, W. Dür, N. Gisin, and N. Sangouard, Rev. Mod. Phys. **90**, 025004 (2018).
[93]We assume that the grating laser is split and the two components are redirected so as to form counter-propagating beams which interfere and form a standing wave. If the standing wave is created by retro-reflecting the grating laser, $n_\pm$ will be twice as large (Ref. 67).
[94]M. Seidl, K.-H. Meiwes-Broer, and M. Brack, J. Chem. Phys. **95**, 1295 (1991).
[95]G. M. Tino, "Testing gravity with cold atom interferometry: results and prospects",Quantum Sci. Technol. **6**, 024014 (2021).

08 May 2026 15:38:38

© Author(s) 2022